IRIS Si IV LINE PROFILES: AN INDICATION FOR THE PLASMOID INSTABILITY DURING SMALL-SCALE MAGNETIC RECONNECTION ON THE SUN

D. E. INNES[1,2], L.-J. GUO[1,2], Y.-M. HUANG[2,3], AND A. BHATTACHARJEE[2,3,4]

[1] Max Planck Institute for Solar System Research, D-37077 Göttingen, Germany; innes@mps.mpg.de
[2] Max Planck/Princeton Center for Plasma Physics, Princeton, NJ 08540, USA
[3] Department of Astrophysical Sciences and Princeton Plasma Physics Laboratory, Princeton University, Princeton, NJ 08540, USA
[4] Center for Heliophysics, Princeton University, Princeton, NJ 08540, USA

ABSTRACT

Our understanding of the process of fast reconnection has undergone a dramatic change in the last 10 years driven, in part, by the availability of high-resolution numerical simulations that have consistently demonstrated the break-up of current sheets into magnetic islands, with reconnection rates that become independent of Lundquist number, challenging the belief that fast magnetic reconnection in flares proceeds via the Petschek mechanism which invokes pairs of slow-mode shocks connected to a compact diffusion region. The reconnection sites are too small to be resolved with images, but these reconnection mechanisms, Petschek and the plasmoid instability, have reconnection sites with very different density and velocity structures and so can be distinguished by high-resolution line-profile observations. Using *IRIS* spectroscopic observations we obtain a survey of typical line profiles produced by small-scale events thought to be reconnection sites on the Sun. Slit-jaw images are used to investigate the plasma heating and re-configuration at the sites. A sample of 15 events from 2 active regions is presented. The line profiles are complex with bright cores and broad wings extending to over $300\,\mathrm{km\,s^{-1}}$. The profiles can be reproduced with the multiple magnetic islands and acceleration sites that characterize the plasmoid instability but not by bi-directional jets that characterize the Petschek mechanism. This result suggests that if these small-scale events are reconnection sites, then fast reconnection proceeds via the plasmoid instability, rather than the Petschek mechanism during small-scale reconnection on the Sun.

Key words: magnetic reconnection – Sun: activity – Sun: transition region – Sun: UV radiation

Supporting material: animations, figure set

1. INTRODUCTION

Magnetic reconnection is the breaking and rejoining of magnetic connections. In space plasmas, it is accompanied by a rapid conversion of magnetic energy into plasma thermal and kinetic energy, and intense particle acceleration. It is fundamental to our understanding of rapid energy release in space plasmas from the Earth's magnetotail (Xiao et al. 2006; Angelopoulos et al. 2008; Nagai et al. 2011) to very remote extragalactic jets (Giannios 2013; Sironi & Spitkovsky 2014). At the Sun, the consequences of reconnection are observed directly in coronal mass ejections (500–1000 Mm), flares (100–300 Mm), and ubiquitous small-scale jets (1 Mm). The Sun therefore provides a range of scales over which reconnection can be studied. Diagnostics rely on images of the high temperature ($\geqslant 10\,\mathrm{MK}$) plasma emissions (Masuda et al. 1994; Aschwanden 2002; Savage et al. 2010; Su et al. 2013), spectra of high velocity jets (Dere et al. 1991; Innes et al. 1997; Winebarger et al. 2002; Imada et al. 2013), radio emission (Nishizuka et al. 2015), and in situ detections of energetic particles (Klassen et al. 2005, 2011).

When reconnection occurs along large aspect-ratio current sheets, structures that appear to look like current sheets with embedded plasmoids have been seen, for example, behind coronal mass ejections (Lin et al. 2005, 2007; Ciaravella & Raymond 2008; Liu et al. 2010; Guo et al. 2013). In large flares reconnection occurs at multiple sites simultaneously and it is difficult to disentangle the dynamics of the reconnection process itself. For this reason, we have investigated small-scale ($\sim$5000 km), short-lived (1–5 minutes) reconnection sites identified by broad non-Gaussian transition region line profiles,

known as transition-region explosive events (Dere et al. 1989). The line-profile evolution during events on the quiet Sun has been shown to be consistent with bi-directional flow (Dere et al. 1991; Innes et al. 1997), as predicted by reconnection models. It was thought that much of the acceleration and heating occurs, as proposed by Petschek (Petschek 1964), along shocks attached to the reconnection region, so that most of the plasma at the reconnection site moves with the Alfvén speed. In the realm of theory, there has been a clear consensus that the Petschek mechanism does not hold unless the resistivity of the plasma is enhanced locally at the X-point (see Biskamp 2000 and other references therein). Despite this theoretical reservation about the Petschek theory, there has been a general tendency to continue comparing observations with the theory. The Petschek model accounts for the high-velocity component but there is insufficient low velocity plasma in the diffusion region to reproduce the strong core brightening that is observed in many events along with the wing enhancements (Dere et al. 1991; Innes 2001). Larger-scale simulations that incorporate surrounding chromospheric and coronal plasma show jets and brightening of the line core from low-velocity plasma outside the diffusion region (Heggland et al. 2009; Ding et al. 2011), so the line core emission has been attributed to heating of the background plasma. In these scenarios, the jet and background emission are spatially off-set which should result in spatial off-sets between the core and wing brightening.

The recently launched *IRIS* spectrometer has significantly higher spatial and spectral resolution than previous solar ultraviolet spectrometers, thus allowing better segmentation of

the reconnection site flows. In addition, high spatial resolution (250 km) co-temporal slit-jaw images show the surrounding transition region and chromospheric heating. Here we focus on active-region events with broad non-Gaussian wings in the Si IV line profile. The Si IV lines are formed over a narrow temperature range around 10^5 K, are optically thin, and change rapidly during transition region heating and acceleration processes.

Extensive studies of similar line profiles seen in the quiet Sun by HRTS (Brueckner & Bartoe 1983; Dere et al. 1989, 1991), and SUMER have shown that they are consistently seen above flux cancellation sites at the boundary of coronal holes (Madjarska et al. 2012), the junctions of supergranule cells (Innes & Teriaca 2013), and during flux emergence (Dere et al. 1991). The line profiles usually show both core and wing enhancements with the wing often preceding the core brightening by about 1–2 minutes (Innes 2001). Sequences of small, fast rasters have shown that in many quiet-Sun events the red and blue wings brighten simultaneously (Ning et al. 2004), although they may be off-set along the slit (Dere et al. 1989; Innes et al. 1997). The active region events sometimes have very complicated line profiles with superimposed narrow absorption lines from singly ionized, neutral and even molecular species (Peter et al. 2014; Schmit et al. 2014).

Although the association with reconnection is widely accepted the actual cause of the line brightening and broad wings is not well understood. Analysis of a quiet Sun explosive event observed by *IRIS* concluded that bi-directional jets were unlikely and suggested plasma ejection and retraction as a plausible scenario (Huang et al. 2014). Here we present a variety of line profiles observed during explosive events and consider reconnection along a thin current sheet subject to the plasmoid instability as an explanation for the profiles seen. The observed line profiles are compared with synthetic profiles from 2D simulations of reconnecting current sheets.

2. OBSERVATIONS

For this study we use high-cadence sit-and-stare *IRIS* observations of Si IV 1402.77 Å taken at full spectral (26 mÅ) and spatial (0.″33) resolution to investigate the time evolution of profiles during explosive events. Context images of the reconnection sites are provided by the *IRIS* slit-jaw camera at 1400 Å, SDO/AIA (Lemen et al. 2012) at 1600 Å and 171 Å, and SDO/HMI (Scherrer et al. 2012) magnetograms. The 1400 Å images reveal sites of bright chromospheric continuum and Si IV transition-region line emission. They can be easily aligned to the AIA 1600 Å images which are also dominated by chromospheric continuum and transition-region line emission. In the quiet-Sun regions most transition-region brightening coincides with 171 Å brightening, but in active regions many of the transition region structures are only seen at wavelengths longward of the Lyman edge at 912 Å because in active regions there is a significant amount of high lying neutral material that is optically thick at wavelengths less than 912 Å due to hydrogen and helium photoionization. Nevertheless there are enough common 1400 and 171 Å features to obtain good image coalignment. The HMI magnetograms were more difficult to coalign. First, we coaligned the 1600 Å to the 1700 Å images. Then, bright structures in the 1700 Å images were matched with small flux concentrations in the magnetograms.
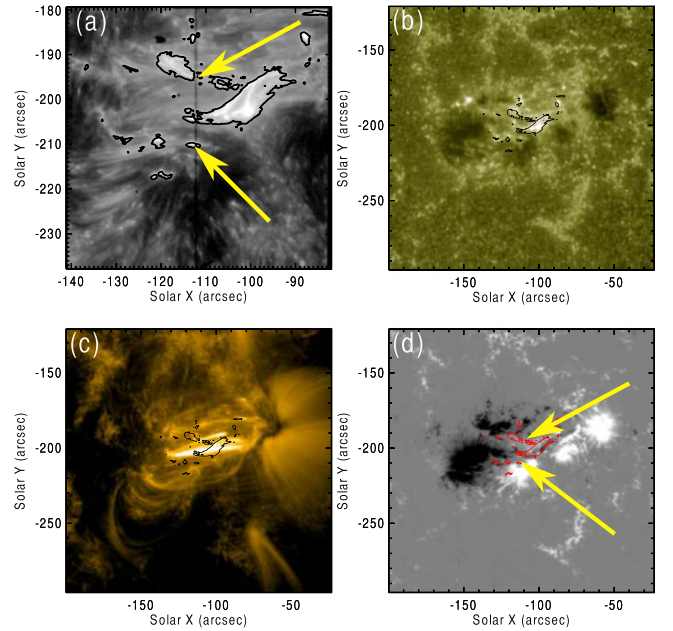

Figure 1. AR 12036 on 2014 April 15 10:22:50 UT: (a) IRIS 1400 Å slit jaw; (b) AIA 1600 Å; (c) AIA 171 Å; (d) HMI line of sight magnetogram. The black vertical line in (a) is the *IRIS* spectrometer slit. All images are overplotted with the same 1400 Å contours at 150 DN s^{-1}. In (a) and (d) the lower yellow arrow points to the site of events 1 and 2, and the upper one to the site of 3, 4, and 5, marked in Figure 2(b).

We show profiles from several sites in two active regions. One was more active and brighter than the other and for this region a shorter exposure time was chosen. The exposure times were 2 and 4 s, and this resulted in time cadences of 3.5 and 5.6 s, allowing for the CCD read-out time (about 1.5 s). In this study, we use sit-and-stare observations which show the evolution of line profiles at a single position. Although this has the disadvantage of measuring flows along a narrow line of sight through the event, rather than showing the flow geometry across the whole event, we obtain better resolution of the profile evolution than would be possible by rastering. The observed profiles can be readily compared to synthetic profiles from comparable slices of the simulated current sheets.

2.1. 2014 April 15 Observations of AR 12036

The first region is a recently emerged active region, AR12036 (Figure 1). It emerged three days earlier, on 2014 April 12, and new flux was still emerging at the time of the observations around 10:00 UT on 2014 April 15. There was a lot of small- and large-scale activity in the region, including a C4.4 flare at 09:53 UT, just 7 minutes before the observations presented here. The bright coronal loops seen in the 171 Å image (Figure 1(c)) connecting positive and negative spots appeared during this flare. The main 1400 Å brightening is below the loops and is visible at 1600 Å but not in the 171 Å or any of the other extreme ultraviolet (EUV) images. The spectrometer slit, shown as a dark vertical line in Figure 1(a), was oriented north–south along the neutral line in the north and across newly emerged positive flux in the south. Both spectrometer and slit-jaw exposures were 2 s and image cadences were 3.5 s.

In Figure 2 we show spacetime maps of the Si IV 1402 Å line intensity and width along the northern half of the slit where
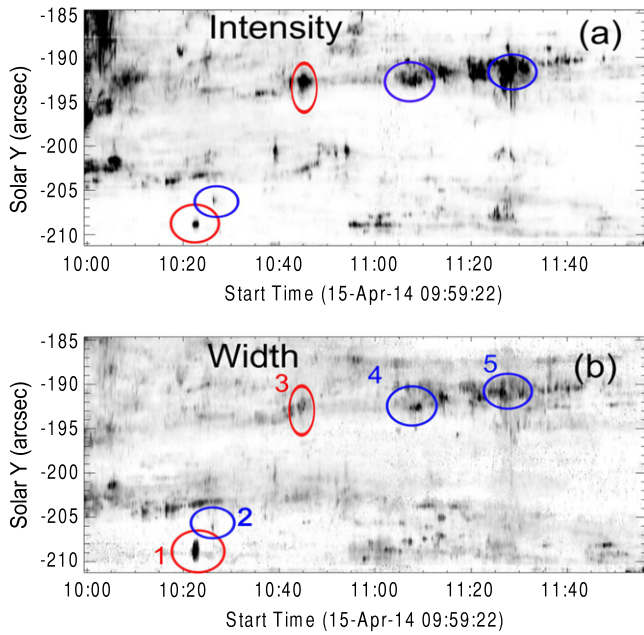
Figure 2. Si IV 1402 Å (a) intensity and (b) width during two hours of sit-and-stare. The maximum values are 2500 DN s^{-1} and 100 km s^{-1}, respectively. The events circled in red are discussed in the main paper. The profiles of those circled in blue are shown in Figure Set 5.
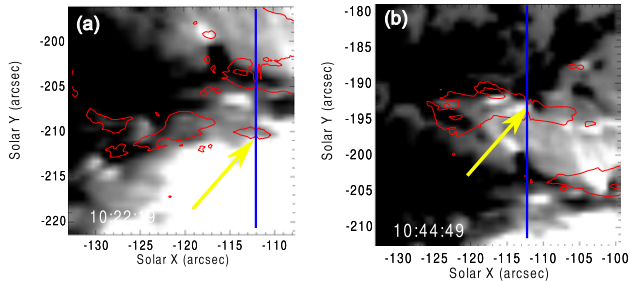

Figure 3. Line of sight magnetic fields near the main sites of Si IV explosive events: (a) the region around the events 1 and 2; (b) the region around 3–5. The blue vertical line indicates the position of the spectrometer slit. Contours are 1400 Å at 100 DN s^{-1}.

Figure 4. Observations of event 1. The top row shows coaligned (a) AIA 171 Å, (b) IRIS 1400 Å slit-jaw, and (c) *IRIS* spectral images around Si IV 1402 Å. The spectral image is overplotted with the line profile from the position marked with a red bar on the left. The other rows show 171 and 1400 Å difference images and spectra at selected times. The site of the event is indicated with yellow arrows in the top row. The red arrow in (e) points to a bright thread, mentioned in the text. The 171 and 1400 Å images are overplotted with the 1400 Å contours at 200 DN s^{-1} from the image taken at the later of the two times given on the 1400 Å difference image. The evolution of the event can also be seen in the movie, *anim1*.

(An animation of this figure is available.)

2.1.1. Transition Region "Jet"

This event, labelled 1, produced the broadest lines of the sequence and occurred at the footpoint of what appeared to be a jet in the 1400 Å slit-jaw images, on the edge of the positive polarity sunspot (Figure 3(a)). The development of the event is shown in Figure 4 and in the movie *anim1*. The top images in Figure 4 show the site, marked by arrows, before the onset of the event. In the following rows, we show difference images that highlight the key structure changes. The corresponding intensity images and the positions of the 1400 Å brightenings with respect to the magnetic field are shown in the associated movie. The first difference images show that the site brightened at 1400 Å but not in 171 Å, indicating that there may be cold material absorbing emission with wavelength shortward of the Lyman limit. The 1400 Å brightening is about 3″.5 in the east–west direction, compared with 1″ along the slit. Since the slit is 0″.33 wide, it only covers about a tenth of the brightening. As seen in (e), the slit cut across the center of the 1400 Å brightening. The brightening coincided with an increase in the line width to 110 km s^{-1} (Figure 4(f)).

most the broad Si IV profiles were seen. Single-Gaussian line-profile fits have been used. The broadest profiles came mostly from sites just north and south of the bright 171 Å loops, where the slit crossed the edge of a region of strong magnetic field, marked with yellow arrows in Figures 1 and 3. After looking at movies of the slit-jaw, AIA and spectral images, we selected what looked like single events and investigated the line profile evolution in more detail. The selected events are circled in the "width" image, Figure 2(b). Red circles surround the two events, described in the next sections, that were particularly interesting because of their evolution in the slit-jaw images. The events were all oriented so that their length in the east–west direction was longer than their width in the north–south direction. Thus the slit crossed a small part of a larger event as seen in the slit-jaw images. The line profiles of the events circled in blue are shown in Figure Set 5. The extent of the broad profiles along the slit is generally only a few pixels, although we show one event (event 5) in the Figure Set that extends about 4″ (24 pixels) along the slit.
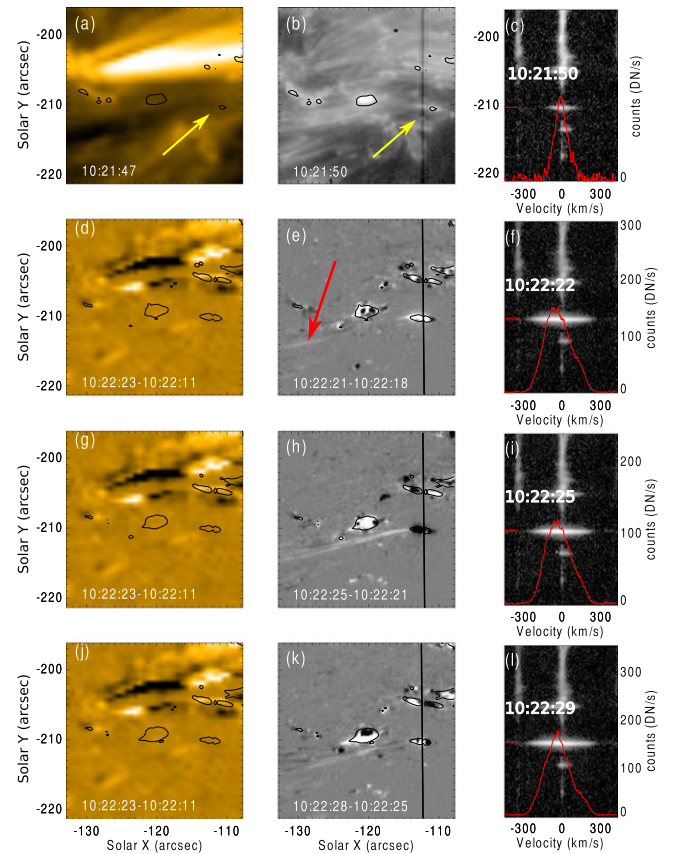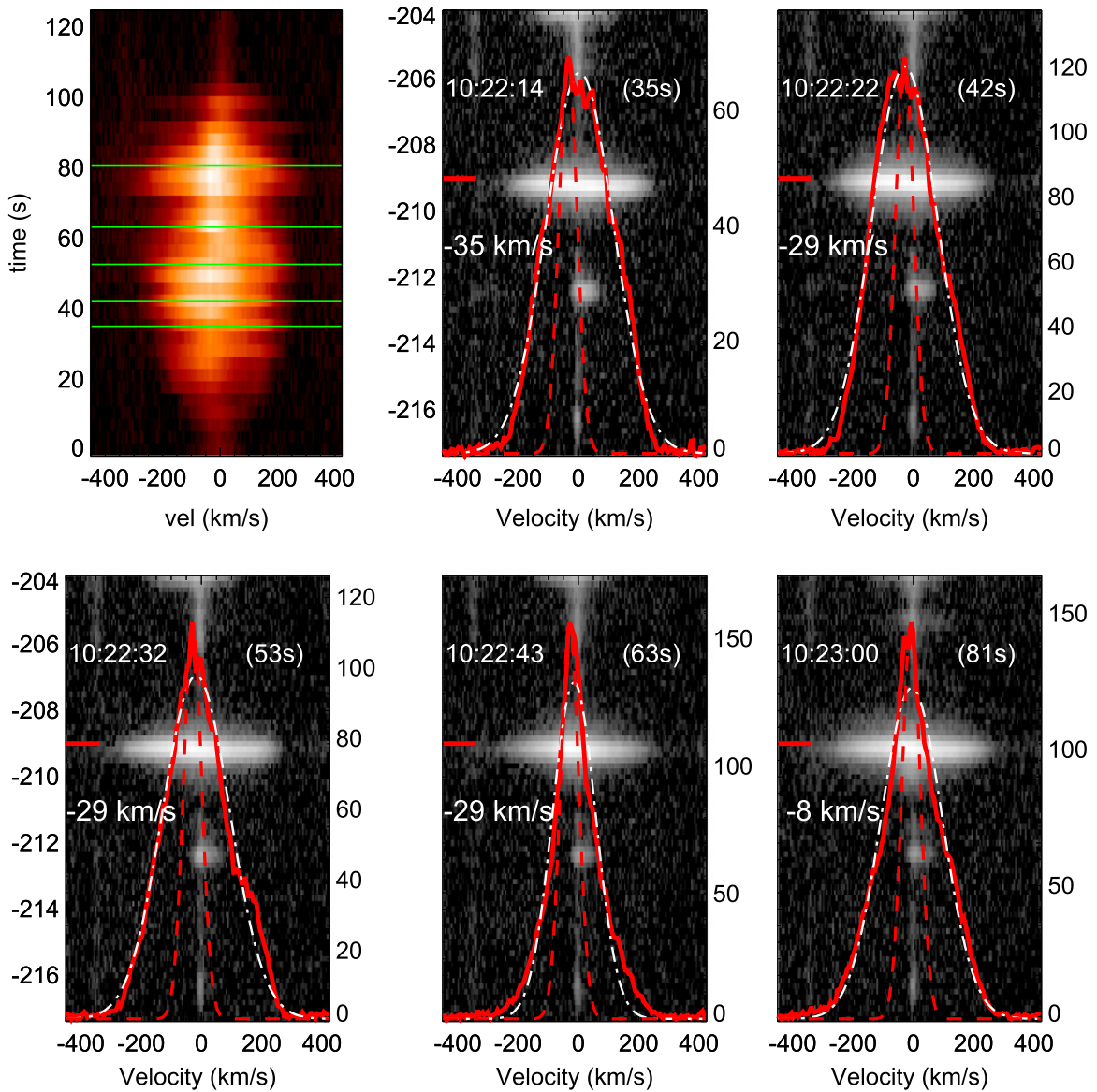
Figure 5. Time evolution of the line profiles during event 1 (similar images of the other events are available in the Figure set). The top left-hand frame shows the time evolution of the profile at the position of the event. Green horizontal lines indicate the times of the spectra in the other frames of the figure. The spectral images show the event structure along the slit (Solar-Y is on the left axis). The profiles are the average over 5 pixels (0″835) at the position of the red horizontal bar on the left. Count rates (DN s^{-1}) are given on the right axis. The narrow, red-dashed profile is a Gaussian with width 30 km s^{-1}, centered at the peak intensity of the line. The velocity shift of the line maximum is given on the left of the profile. The white dotted–dashed line is the best-fit Gaussian.

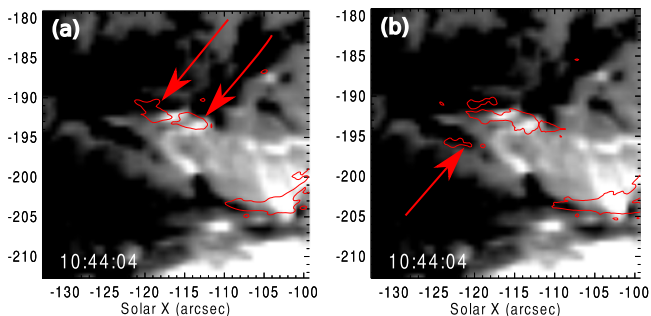(The complete figure set (11 images) is available.)

Figure 6. Relation between magnetic field and 1400 Å during event 3. The red contours are the 1400 Å intensity at 200 DN s^{-1}. The arrows in (a) point to 1400 Å sites above adjacent positive and negative flux. The arrow in (b) points to the footprint of the new 171 Å loop.

A jet-like structure leading directly from the bright site appears in the next difference image (Figure 4(h)). It is hard to measure the extent of the jet because it blends with a similar narrow 1400 Å thread seen in the earlier difference image (red arrow in (e)). Assuming that the jet ends before this thread, its length is 9″. Given the time between slit-jaw images, 3.5 s, the speed of the jet would be about 2000 km s^{-1} which is extremely fast for transition region plasma. We suggest two possible explanations. The first is that the thread was heated to a higher temperature and cooled rapidly along its length thus giving the impression of a fast jet. The second is that the thread is heated by high energy particles generated in the reconnection region that precipitated along a thread-like structure while propagating away from the reconnection site. The only evidence for earlier heating is the flare at 9:53 UT. This may be related but because the flare emission is clearly separated
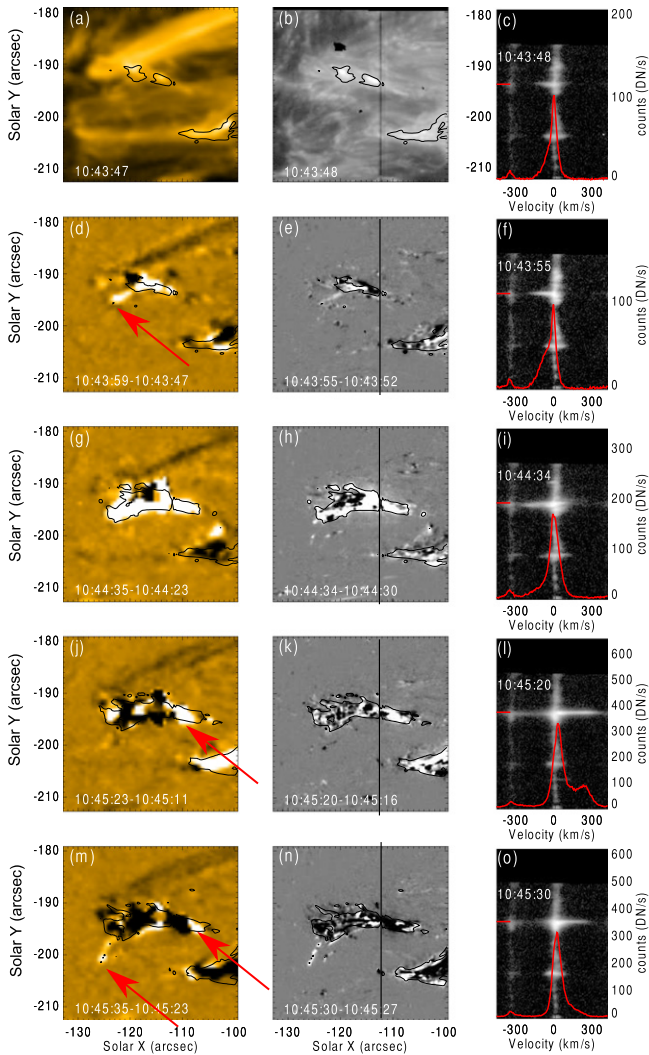
Figure 7. Evolution of event 3. For a description of the images see Figure 4. The arrow in (d) points to a new 171 Å loop. The arrow in (j) points to a brightening west of the slit that may be related to redwing enhancements in the spectra. The arrows in (m) point to plasma outflows with a plane-of-sky velocity about 250 km s^{-1}. The evolution of the event can also be seen in the movie, *anim3*.

(An animation of this figure is available.)

from the thread, we think that the second explanation is most likely, in which case the observed brightening and broad line profiles at the footpoint were due to reconnection. The geometry of the jet and flows are quite a puzzle because the broad line profiles extend out to 300 km s^{-1} which is close to the Alfvén velocity, so we expect that the reconnection flow would be toward and away from the observer; however the jet is seen perpendicular to the line of sight. Some more comments on the jet's appearance and an energy estimate for the particles is given in the discussion section.

The line profile during the evolution of this event is shown in Figure 5. Broad wings are seen for 90 s, and extend out to ± 300 km s^{-1}. During the first 30 s of the event, the core and wings brighten simultaneously and the profile is close to Gaussian (white dotted–dashed line) with a width of about 110 km s^{-1}. After about 10:22:32 UT, the core intensity relative to the wings increases and it is no longer possible to fit both the core and wing with a single Gaussian. The core

component is well represented by the red-dashed line showing a Gaussian with width 30 km s^{-1}. Like the turbulent events first reported by Brueckner & Bartoe (1983), the profiles are symmetric and there is no offset of the red and blue components along the slit.

2.1.2. Loop Reconfiguration

The second event, labelled 3, occurred on the edge of the negative sunspot (Figure 3(b)). The event was significantly larger than event 1, and its EUV emission was not obscured by intervening cold material so that it was visible in both the 171 and 1400 Å images. Before the event there were just two small elongated 1400 Å emission sites on the edge of the negative field (red arrows in Figures 6(a), 7(b)). At event onset, a finger of 171 Å emission appeared connecting these sites to negative flux in the south (red arrow in Figures 6(b), 7(d)), suggesting that reconfiguration had occurred. The evolution is best seen in the movie, *anim3*, of this event. The profile evolution is shown in Figure 8. Initially the blue wing dominates. Subsequently the line core brightens by a factor three. Both blue and red-wing enhancements are seen with the red wing north of the blue by 0″.33 (2 pixels). Between 10:45:23 and 10:45:11 UT (Figure 7(j)) a bright knot of emission appears on the west of the slit. It seems to be related to the red-wing enhancements seen at that time. At the end of the sequence, blobs are seen in the 171 and 1400 Å images moving both to the south and west with a plane-of-sky velocity 250 km s^{-1} (Figure 7(m)).

The sequence of wing enhancements could be interpreted as the ejection and retraction of plasma (Huang et al. 2014), and the line-core brightening when the red-wing enhancements appear could be explained as plasma compression at the site of the returning plasma. However, as we point out in the discussion section, both the red and blue-wing enhancements could also be due to reconnection outflows, especially as the images show clear evidence for reconfiguration and oppositely directed plane-of-sky flows at the end of the sequence.

2.2. 2014 May 03 Observations of AR 12049

The second active region, AR12049, shown in Figure 9 was quieter. There was a large leading positive spot separated by about 50″ from two trailing negative spots. The previous significant flare from this region had been a C1.5 two and a half days earlier. The *IRIS* spectrometer slit was orientated north–south between the positive and negative polarity spots. *IRIS* observations were taken over a period of 3 hr, with an exposure time of 4 s, and a time cadence of 5.6 s for the spectra and 11 s for the 1400 Å slit-jaw images.

In Figure 10 we show the Si IV 1402 Å line intensities and widths. There were many small, apparently isolated, events. The events characterized by enhanced line wings were mostly at three positions along the slit. They coincide with the regions of mixed-polarity field observed by the spectrometer. As examples we show in the next section events, circled in red, from two of the sites. Line profiles from the events inside blue circles are shown in Figure Set 5. The part of the slit covering strong positive field ($-50″ <$ Solar Y $< -35″$) detected many brightenings without broad wings. The part of the slit covering weak field ($-70″ <$ Solar Y $< -60″$) showed neither intensity variations nor line broadening.
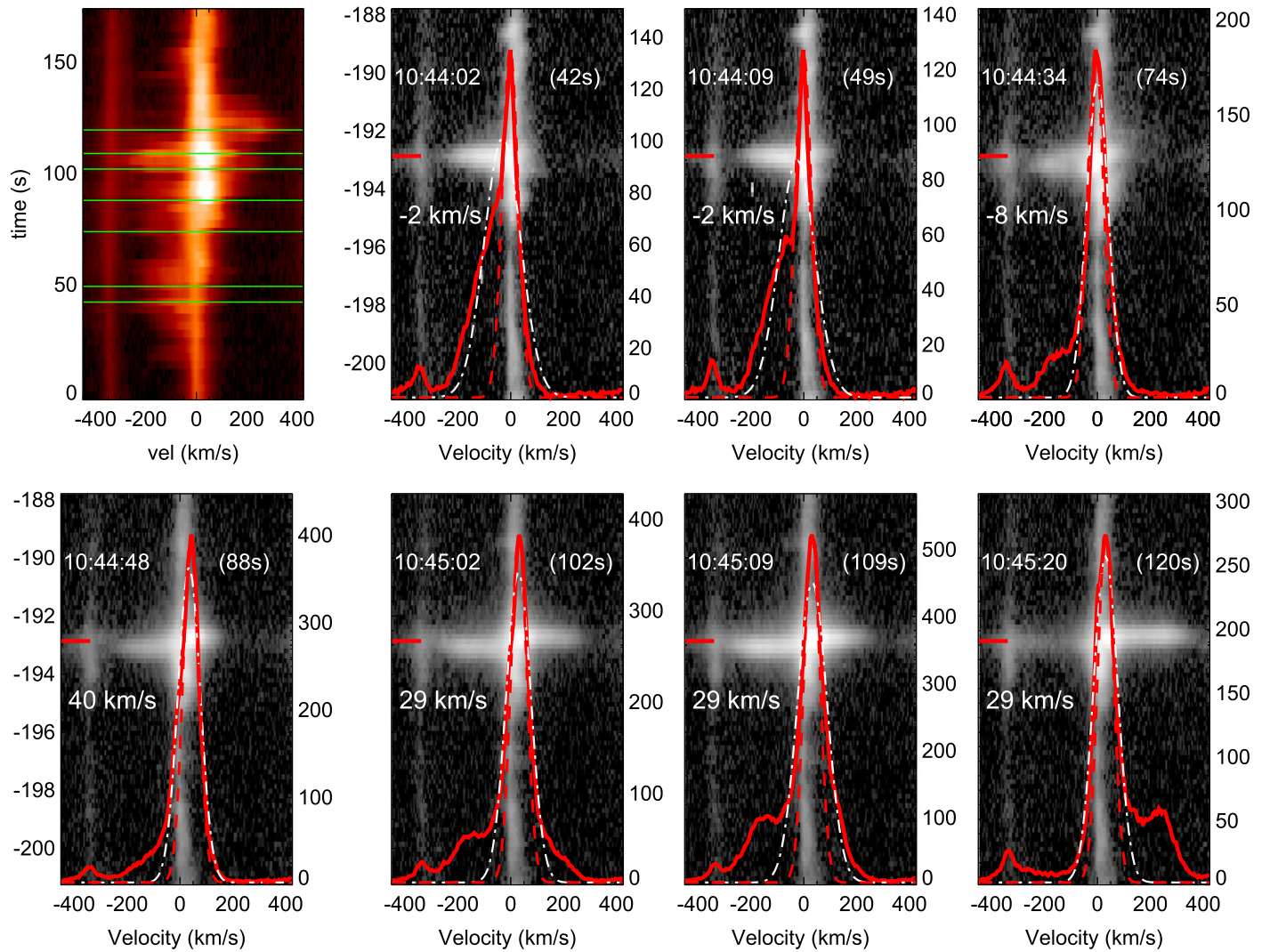
Figure 8. Time evolution of the line profiles during event 3. For a description of the images see Figure 5.

2.2.1. Multiple Small Jets

The site with mixed-polarity field, shown in Figure 11(a), produced a series of small events in the 3 hr of observation. Although we did not measure the cancellation of photospheric flux, the magnetic configuration was favourable for reconnection in the atmosphere above. Here we show and discuss the evolution of the last and largest event, event 9, from this site. The line profiles of events marked 6, 7, and 8 are shown in Figure Set 5.

Selected images and spectra of event 9 are shown in Figure 12. The full event is shown in the movie, *anim9*, and the evolution of the line profile in Figure 13. It was not one continuous event but consisted of four events with lifetime of about 50 s and two very short ones with a lifetime about 10 s. During most of the events the slit is on the eastern edge of the brightening and the profile was distinctly non-Gaussian with a dominant blue-wing enhancement, suggesting that the slit is crossing the upward propagating part of the reconnection outflow. The last profile in Figures 12 and 13 has an intense blue peak around $100 \, \text{km s}^{-1}$, tailing off to a broad, low-intensity red wing extending to $200 \, \text{km s}^{-1}$, as though the up- and downflows were continuous. This is unusual because

normally when both blue and red wings are present, they are separated by a bright core.

The profiles from the other events from this site are shown in Figure Set 5. They all show stronger blue wings than red. This is consistent with outward directed jets being on the east of the brightening where we see a bigger extension in the images. We note that in the EUV images, the site was initially dark and brightenings were not seen, indicating that neutral material in the upper atmosphere obscured the emission at these wavelengths.

2.2.2. EUV Brightening

This event is noteworthy because in spite of being inside a dark EUV lane, it was seen in the EUV (Figure 14 and *anim14*). It occurred on the edge of positive polarity flux near the north of the slit (Figure 11(b)). The event was relatively small with a lifetime of about 60 s. It started with a clear blue-wing enhancement and brightening at 1400 and 171 Å. Then, as shown in Figure 15, the line core increased in intensity and the enhanced wings became more symmetric. Although the 11 s cadence was a bit slow to pick up movement, the slit-jaw running-difference images did show increased emission in both
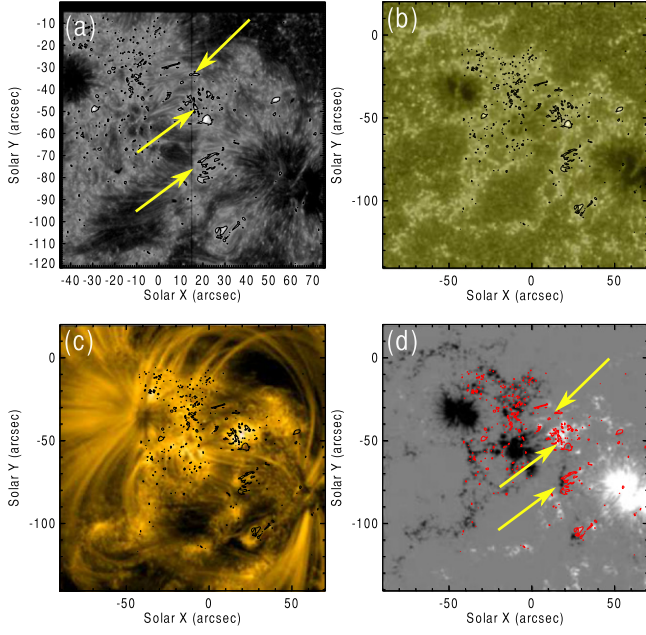
Figure 9. AR 12049 on 2014 May 03 13:35:18 UT, site of events 6–15: (a) IRIS 1400 Å slit jaw; (b) AIA 1600 Å; (c) AIA 171 Å; (d) HMI line of sight magnetic field. The black vertical line in (a) is the *IRIS* spectrometer slit. All images are overplotted with the same 1400 Å contours. In (a) and (d) the yellow arrow points to the three main event sites.
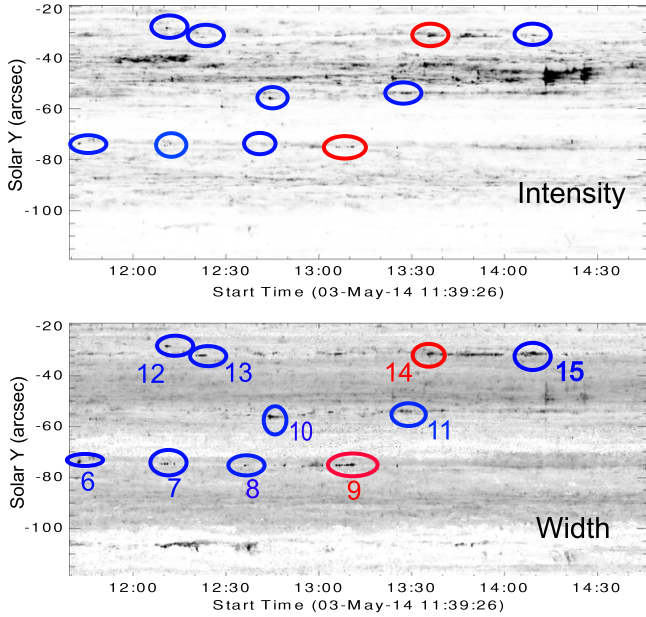

Figure 10. Si IV 1402 Å (a) intensity and (b) width during three hours of sit-and-stare. The maximum values are 1000 DN s^{-1} and 100 km s^{-1}, respectively.

the east and west directions (Figure 14(h) and *anim14*) which could be caused by plasma motion away from the event center.

3. DISCUSSION

Altogether we show the evolution of Si IV lines profiles from 15 events, from 2 active regions, with the aim of obtaining an overview of typical explosive event behavior. The evolution of two events from each active region is described in the main paper and profiles for the other events are shown in Figure
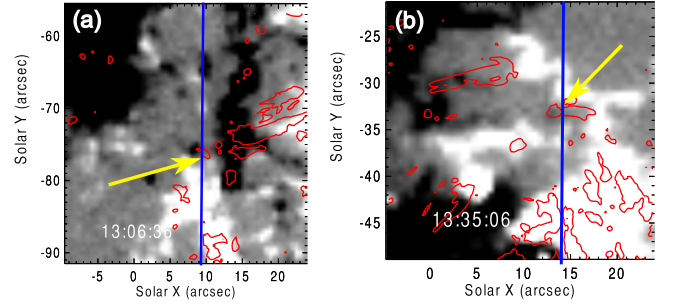

Figure 11. Magnetic field at the sites of (a) event 9 and (b) event 14. The red contours are the 1400 Å intensity at 100 DN s^{-1}.
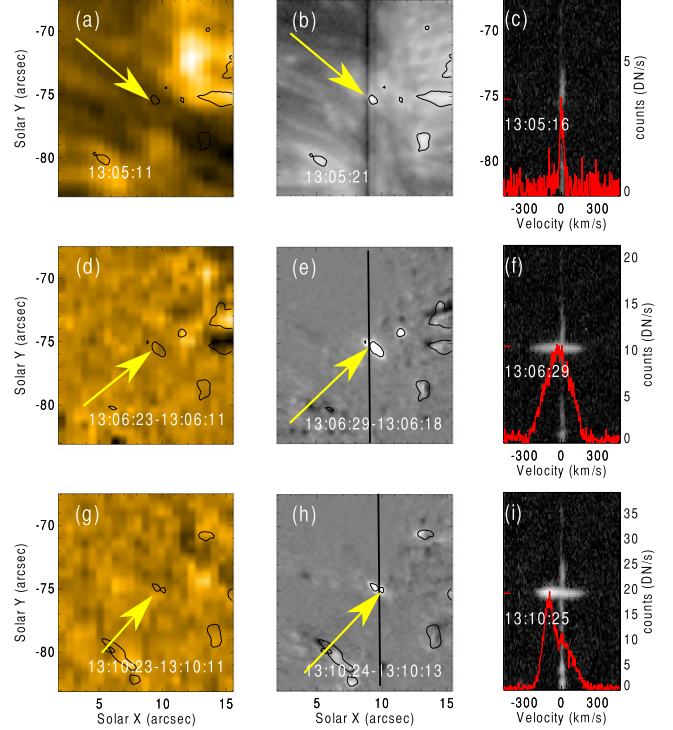

Figure 12. Observations of event 9. For a description of the images see the caption of Figure 4. The contours are at 1400 Å 100 DN s^{-1}. The event evolution is shown in the movie, *anim9*.

(An animation of this figure is available.)

Set 5. We have used sit-and-stare observations and show the full profiles to emphasize the flow structure along a single line of sight rather than the energetics.

The properties of explosive events have been frequently reported but there is still no clear consensus on the profile evolution or their interpretation. Because the sites of line broadening are found at the boundary of strong field regions or close to the neutral line of magnetic bipoles, they are thought to result from magnetic reconnection. In this study we found all sites were on the edge of strong field regions, and at half the sites neighboring opposite polarity field was also present. The slit-jaw images always showed brightening at the site and, in several cases, elongation of the emission structures in opposite directions away from the event center (events 3 and 14). These motions were perpendicular to and had a shorter lifetime (<10 s) than the observed Doppler flows, so they were not the explosive event flows but showed that there was some movement of plasma across the solar surface as well.
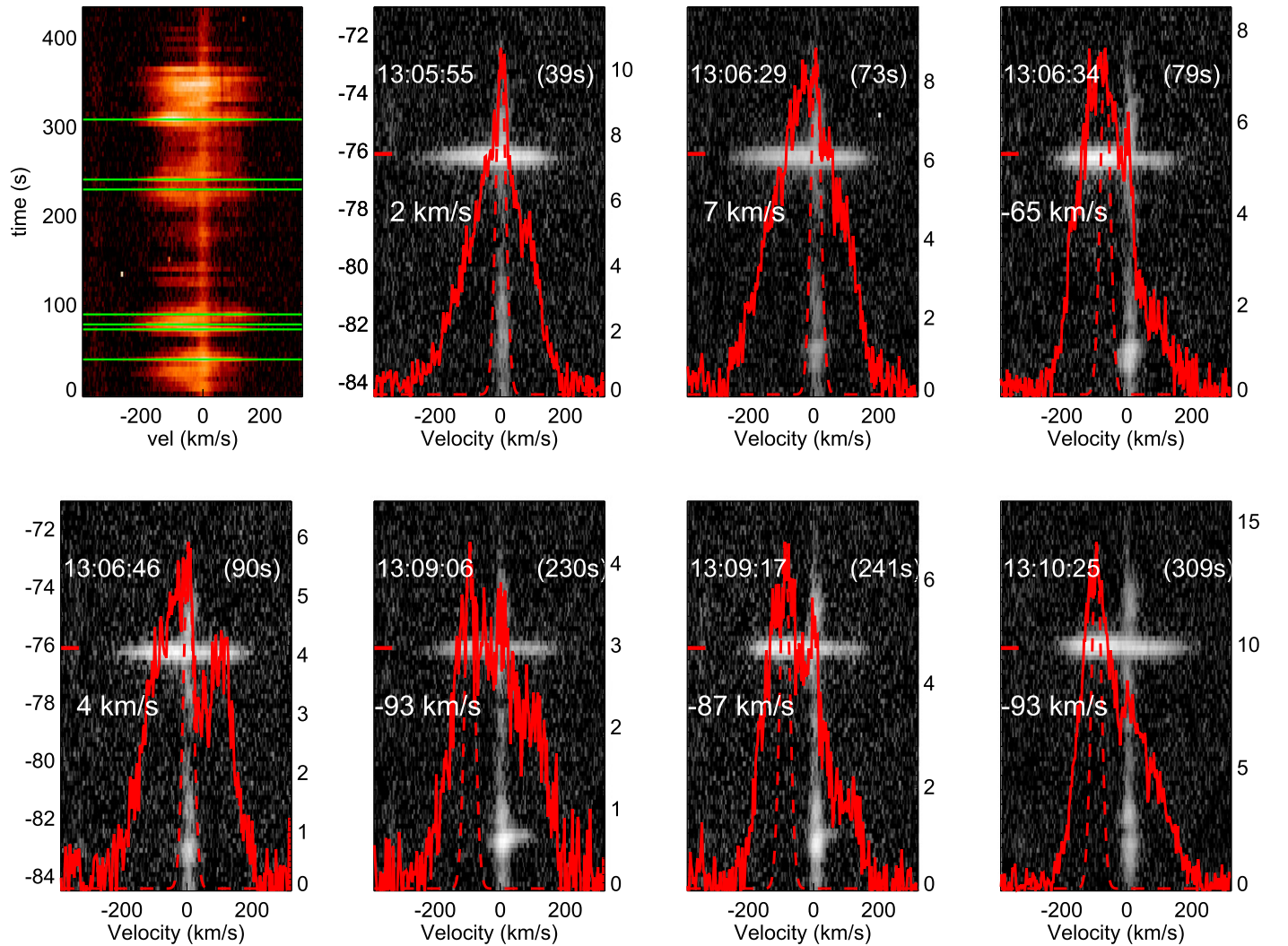
Figure 13. Time evolution of the line profiles during event 9. See the caption of Figure 5 for a description of the images.

The most surprising of the slit-jaw observations is the jet-like extension that suddenly appeared connected to explosive event site 1 (Figure 4). As mentioned in Section 2.1.1, the "jet" was about 10 times faster and perpendicular to the explosive event flows. We therefore attribute it to a process other than flows, possibly heating by energetic particles. An estimate of the appropriate particle energies can be obtained by considering electrons with energy $\epsilon = 2\,\mathrm{keV}$, interacting with plasma of density $n = 10^{10}\,\mathrm{cm}^{-3}$. The collision rate is about $4 \times 10^{-6}\epsilon^{-3/2}n \ln \Lambda\,\mathrm{s}^{-1} = 4.5\,\mathrm{s}^{-1}$, where $\ln\Lambda$ is the coulomb logarithm which has a value of about 10 (Huba 2004). Such particles will travel roughly 6 Mm equivalent to 8″ in their 0.2 s lifetime. Thus if particles can be accelerated to about 2 keV in the source region which is quite feasible given the efficiency of particle acceleration, heating by energetic particles is not an implausible explanation for the thread. However, it is not easy to understand why only this narrow thread brightened at 1400 Å. It may be an effect of the coronal (guide) field, or non-uniformities in either the source region or adjacent loops. Further observations are required to find out how frequently these jet-like structures are seen.

For this study, we note that if it is caused by energetic particles then the Si IV emission is likely from a reconnection site, and the line profile gives information about the velocity and density distribution in the reconnection region. Previous reconnection models have concentrated on reproducing the highest observed velocities (Dere et al. 1991; Innes & Tóth 1999; Roussev et al. 2001). One of the issues not previously addressed is the cause of the low velocity intensity increase observed as bright line cores. In this study, most profiles have a narrow core with low intensity wings extending out to about 200 km s^{-1}(e.g., the profiles in events 2, 3, 4, 5, 10, 11, 13, 14, 15). In most events core brightening was seen soon after event onset (events 1, 2, 3, 5, 10, 11, 12, 13, 14). In fact, the only events that did not show significant core brightening were events 6–9. These were all from the same site and were the only ones with the line peak significantly shifted (>50 km s^{-1}) to the blue, so the reason may be due to the geometry of the event and how the slit crossed the site. As seen in Figure 12, the slit was on the edge of event 9. Events 10 and 11 had an extended red but very little blue wing throughout their evolution. Both were from the same site so this again suggests that the position of the slit with respect to the site is important. In two events the red wing develops at the end of the event (3, 5). Both these events were large complex events, making them difficult to interpret. We note that in none of the events did the site of the explosive event move along the slit (in the north–south direction) suggesting that the process causing
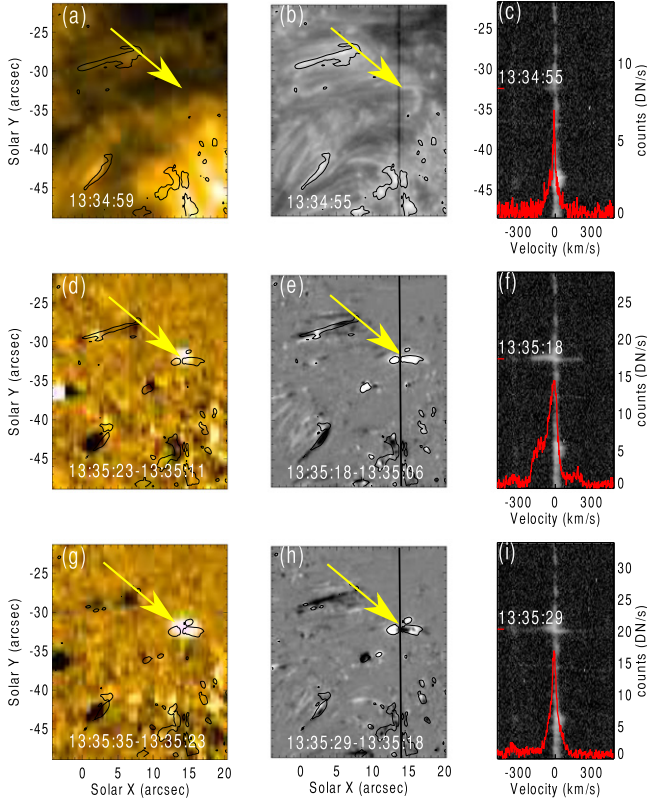
Figure 14. Observations of event 14. See caption of Figure 4 for a description of the images. The event evolution is shown in the movie, *anim14*.

(An animation of this figure is available.)

Figure 15. Time evolution of the line profiles during event 14. See caption of Figure 5 for a description of the images.

the shifts occurs at a stationary site. In addition the core and wing emission coincide along the slit, which suggests that they are produced by the same structure not by heated chromospheric plasma below the jet.

We now assume that the basic cause is reconnection and test whether the line profiles can, at least qualitatively, be reproduced by reconnection models. Previous models of fast reconnection in the transition region (Innes & Tóth 1999; Roussev et al. 2001) have used anomalous resistivity at a single site to generate pairs of slow-mode shocks (Petschek 1964). Recently it has become clear that current sheets are unstable to plasmoid formation (Loureiro et al. 2007; Bhattacharjee et al. 2009; Huang & Bhattacharjee 2013) with a linear growth rate that scales with the Lundquist number, S, as $S^{1/4}$ and a nonlinear reconnection rate that is independent of S (Bhattacharjee et al. 2009; Huang & Bhattacharjee 2010; Uzdensky et al. 2010) in comparison to the Sweet–Parker rate that scales with $S^{-1/2}$. So in high Lundquist number plasmas such as the solar transition region where $S \sim 10^{10}$, the short-lived linear regime of the plasmoid instability can witness fast, exponential growth leading to a nonlinear regime in which multiple islands of dense, low-velocity plasma can be produced. Each island has an o-point in its center and a pair of x-points at its sides where plasma is accelerated. The formation and interaction of multiple islands in the current sheet leads to velocity distributions (Uzdensky et al. 2010; Huang & Bhattacharjee 2012; Loureiro et al. 2012) that may produce bright cores and enhanced wings.

Results from two-dimensional (2D) simulations of reconnection along a Harris sheet at Lundquist number 10^5 are shown in
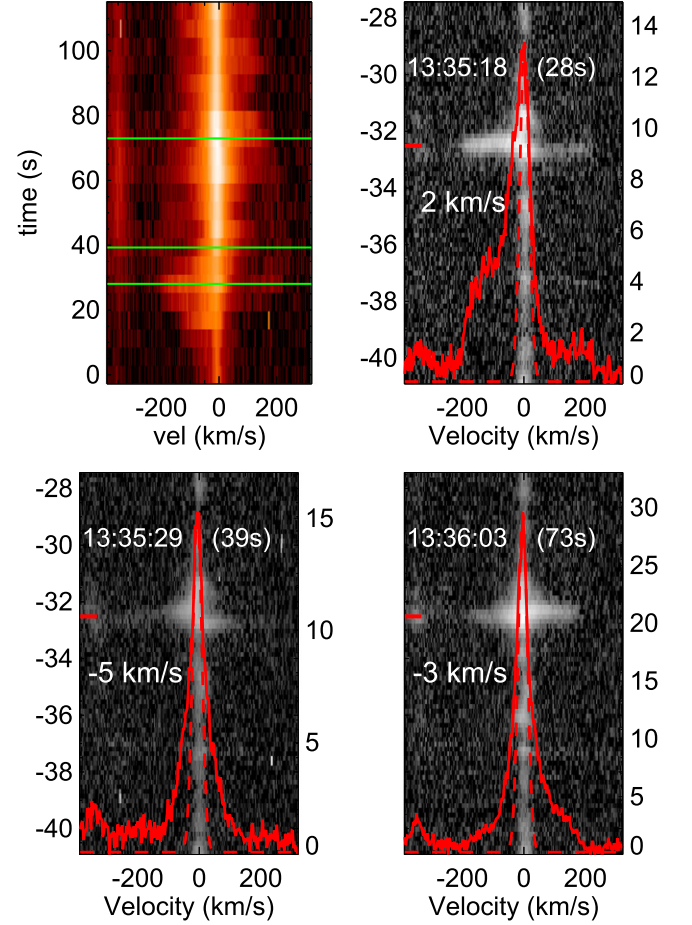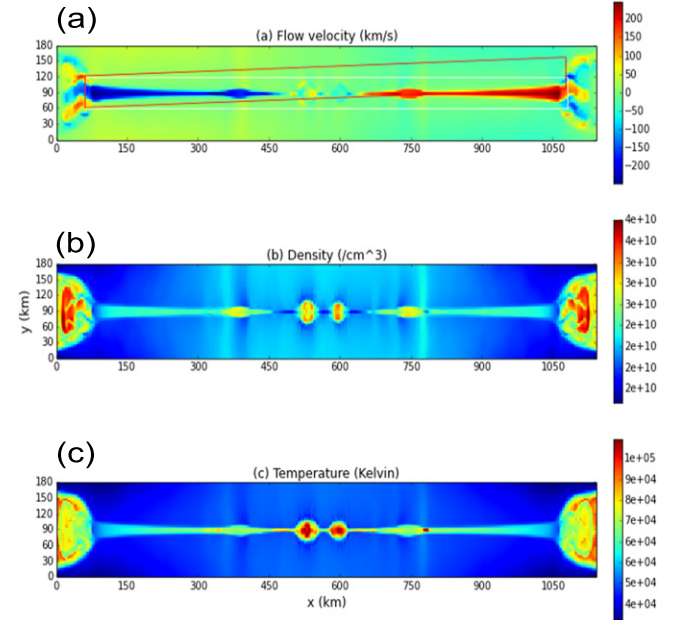

Figure 16. Simulation of reconnecting current sheet: (a) velocity (b) density (c) temperature. The white box in (a) shows the region that produced profiles Figures 17(b)–(d), and the red box the region that produced (e)–(g). The integration was along the long axis of the boxes.
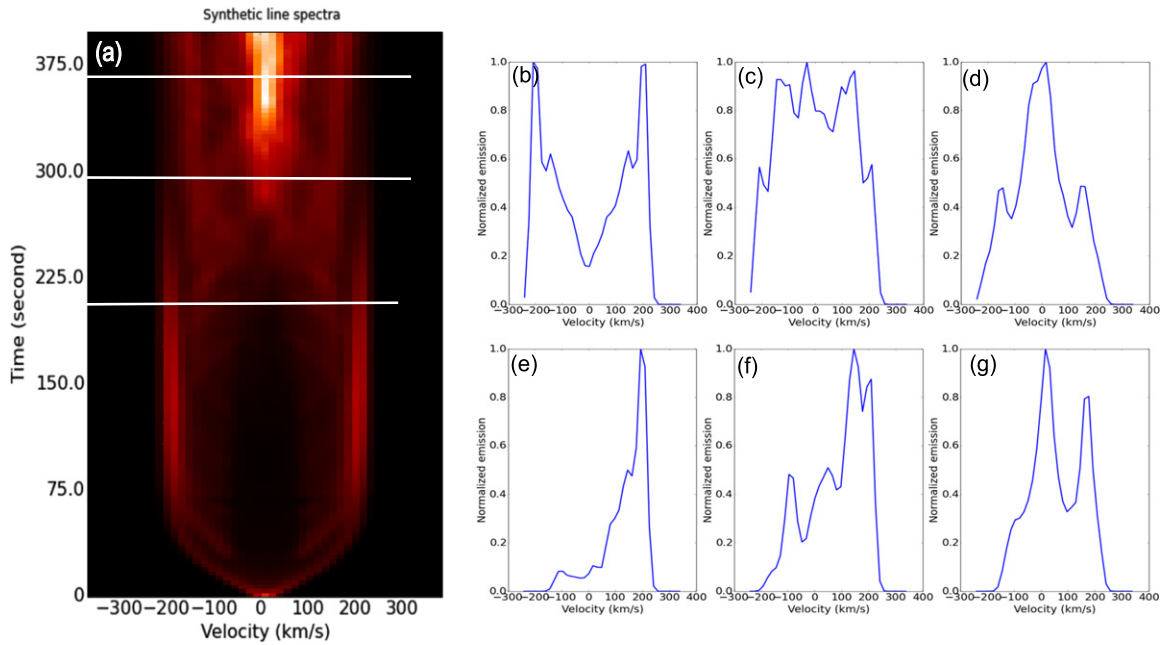
Figure 17. Line profiles from simulations of a 2D current sheet with $\beta = 0.1$: (a) time evolution of the line profile of a line formed around 8×10^4 K, with line of sight along the current sheet (white box in Figure 16(a)). The white horizontal lines indicate the times at which the profiles on the right are taken. The top row shows profiles along the current sheet (white box) and the bottom integration along the line of sight at a slight angle (red box).
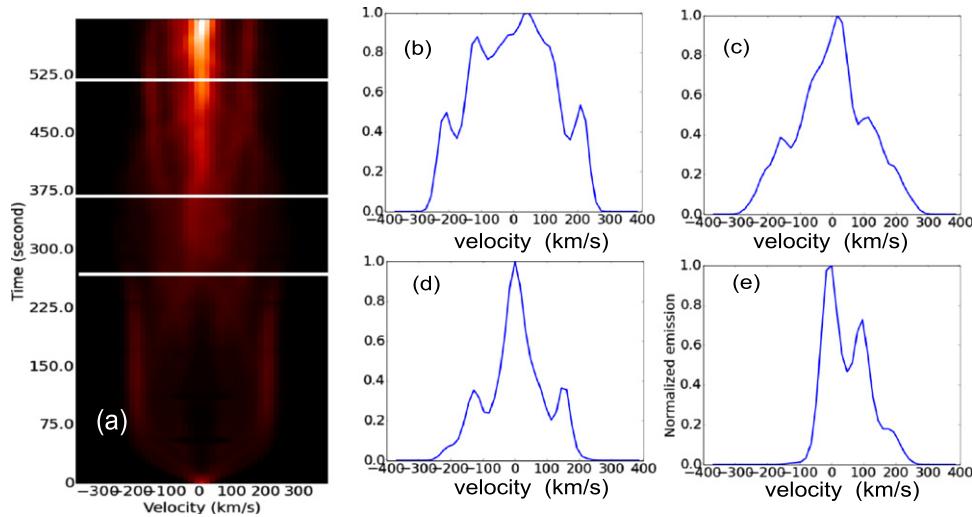

Figure 18. Line profiles from simulations of a 2D current sheet with $\beta = 0.5$: (a) time evolution of the line profile of a line formed around 5×10^5 K with line of sight along the current sheet. The white horizontal lines indicate the times at which the profiles (b)–(d) are taken. The profile (e) is taken along a line of sight at a small angle to the current sheet at the time of (d).

Figure 16. The simulations have been done with the Athena code (Stone et al. 2008), using the double current-sheet setup described in Hawley & Stone (1995), and a grid with 200 cells along the sheet and 400 across it. The setup did not include a guide field. Reconnection along the current sheet is triggered with a small magnetic perturbation along the current sheet, as described in Guo et al. (2014). Small, random velocity perturbations throughout the domain are used to initiate the instability. The asymptotic values are plasma beta, $\beta = 0.1$, inflow number density $n = 10^{10}\,\mathrm{cm}^{-3}$, and magnetic field $B = 12\,\mathrm{G}$ which gives an Alfvén speed in the inflow region, $V_A = 250\ \mathrm{km\,s}^{-1}$ and temperature, $T = 2 \times 10^5\,\mathrm{K}$. Our simulation parameters are a compromise between what the observations require and what is computationally feasible. For example the Lundquist number is much smaller than that of the

Sun. This means that the linear instability growth rate is about a factor 10 too slow. Ohmic heating is included but radiative cooling and conduction are not which makes the simulated temperatures rather high. Nevertheless the current sheet structure which produces the line-profile characteristics should remain even when these processes are included.

Figure 16 shows the velocity, number density, and temperature along the current sheet just after the onset of plasmoid formation when there are about 3–4 well-separated plasmoids along the sheet. Each of the central high-density, low-velocity islands is separated by bi-directional high-velocity jets. In both directions the maximum plasma velocity is of the order the Alfvén speed which in active regions is about 200–$300\ \mathrm{km\,s}^{-1}$. Synthetic transition region (e.g., Si IV) line profiles are shown in Figure 17. For calculating line intensity

we assume a top-hat function that is one between 6×10^4 and 1×10^5 K and zero everywhere else, and a Gaussian line width based on the plasma temperature. Initially reconnection produces oppositely directed jets similar to Sweet–Parker reconnection, seen as well-separated red and/or blue wings in the line profile 17(b). Then the current sheet becomes unstable and breaks up into several small plasmoids moving at different velocities reflected in the line profiles as broad, multi-component profiles (17(c)). About 1 minute later, the smaller plasmoids merge giving rise to broad profiles with a bright core component (17(d)). Depending on the integration path, profiles with different core-to-wing ratio and asymmetry are obtained. In the bottom row of Figure 17, we show profiles obtained by integration along the red box in Figure 16(a) at the same times.

The island characteristics are affected by plasma beta, grid resolution, and Lundquist number. An increase in any of these parameters leads to smaller islands and smoother wings. Examples of profiles from a $\beta = 0.5$ run is shown in Figure 18. Since temperature scales with β, the temperature of the line shown here is 5×10^5 K. Explosive event profiles are seen frequently in lines such as O VI and Ne VIII which are formed at these higher temperatures (Winebarger et al. 2002).

Although this simulation is not realistic because it is only 2D and does not include radiative losses or conduction, it gives a qualitative idea of how plasmoid formation might affect the line profiles. They have much better agreement with observations than profiles from Petschek or Sweet–Parker reconnection which only have strong wing brightening (Innes & Tóth 1999; Roussev et al. 2001), or larger-scale, low-resolution computations that have distinct jet and background core components (Ding et al. 2011).

In reality the magnetic configuration is more complicated and non-uniformities at the reconnection site are likely to contribute to the line profiles. The point we would like to emphasize is that island formation, and hence the plasmoid instability as a self-contained model, is able to explain some of the principle features of the observed profiles in the context of reconnection. The next step is to investigate raster observations with *IRIS* to deduce the flow geometry of events, and develop more realistic simulations that include conduction, radiative cooling and a realistic solar atmosphere. Our MHD simulations will need to be augmented by kinetic simulations in order to make connections with the physics of particle acceleration and heating.

4. CONCLUSION

The line profiles at small-scale acceleration sites in active regions consistently show broad, low-intensity red and/or blue wings extending to $200 \, \mathrm{km \, s^{-1}}$, and a bright central core. The core with a width of about $30 \, \mathrm{km \, s^{-1}}$ tends to brighten after the first appearance of the wing emission. The core and wing emission are spatially coincident and neither move significantly during the typically 2–5 minutes event duration. Thus both components seem to come from the same stationary site. It has long been speculated because of their association with cancelling magnetic flux that these line broadenings are caused by small-scale magnetic reconnection. Previous reconnection models based on the Petschek mechanism were able to reproduce the wing but not the core emission. We suggest that the core emission is from high-density, low-velocity magnetic islands that form due to the plasmoid instability along the current sheet under high-Lundquist-number solar conditions. Our 2D-MHD simulations of magnetic reconnection show the rapid growth of magnetic islands along the current sheet. The islands are

separated by fast jets and can explain both the core and wing components of the observed line profiles. We conclude that the *IRIS* line profiles could result from reconnection via the plasmoid instabilty during small-scale events on the Sun.

REFERENCES

Angelopoulos, V., McFadden, J. P., Larson, D., et al. 2008, Sci, 321, 931
Aschwanden, M. J. 2002, SSRv, 101, 1
Bhattacharjee, A., Huang, Y.-M., Yang, H., & Rogers, B. 2009, PhPl, 16, 112102
Biskamp, D. 2000, Magnetic Reconnection in Plasmas (Cambridge University Press)
Brueckner, G. E., & Bartoe, J.-D. F. 1983, ApJ, 272, 329
Ciaravella, A., & Raymond, J. C. 2008, ApJ, 686, 1372
Dere, K. P., Bartoe, J.-D. F., & Brueckner, G. E. 1989, SoPh, 123, 41
Dere, K. P., Bartoe, J.-D. F., Brueckner, G. E., Ewing, J., & Lund, P. 1991, J. Geophys. Res., 96, 9399
Ding, J. Y., Madjarska, M. S., Doyle, J. G., et al. 2011, A&A, 535, A95
Giannios, D. 2013, MNRAS, 431, 355
Guo, L.-J., Bhattacharjee, A., & Huang, Y.-M. 2013, ApJL, 771, L14
Guo, L.-J., Bhattacharjee, A., Huang, Y.-M., & Innes, D. E. 2014, arXiv
Guo, L.-J., Huang, Y.-M., Bhattacharjee, A., & Innes, D. E. 2014, ApJ, 796, L29
Hawley, J. F., & Stone, J. M. 1995, CoPhC, 89, 127
Heggland, L., De Pontieu, B., & Hansteen, V. H. 2009, ApJ, 702, 1
Huang, Y.-M., & Bhattacharjee, A. 2010, PhPl, 17, 062104
Huang, Y.-M., & Bhattacharjee, A. 2012, PhRvL, 109, 265002
Huang, Y.-M., & Bhattacharjee, A. 2013, PhPl, 20, 055702
Huang, Z., Madjarska, M. S., Xia, L., et al. 2014, ApJ, 797, 88
Huba, J. D. 2004, NRL Plasma Formulary (Washington: Naval Research Laboratory)
Imada, S., Aoki, K., Hara, H., et al. 2013, ApJL, 776, L11
Innes, D. E. 2001, A&A, 378, 1067
Innes, D. E., Inhester, B., Axford, W. I., & Wilhelm, K. 1997, Natur, 386, 811
Innes, D. E., & Teriaca, L. 2013, SoPh, 282, 453
Innes, D. E., & Tóth, G. 1999, SoPh, 185, 127
Klassen, A., Gómez-Herrero, R., & Heber, B. 2011, SoPh, 273, 413
Klassen, A., Krucker, S., Kunow, H., et al. 2005, JGRA, 110, 9
Lemen, J. R., Title, A. M., Akin, D. J., et al. 2012, SoPh, 275, 17
Lin, J., Ko, Y.-K., Sui, L., et al. 2005, ApJ, 622, 1251
Lin, J., Li, J., Forbes, T. G., et al. 2007, ApJL, 658, L123
Liu, R., Lee, J., Wang, T., et al. 2010, ApJL, 723, L28
Loureiro, N. F., Samtaney, R., Schekochihin, A. A., & Uzdensky, D. A. 2012, PhPl, 19, 042303
Loureiro, N. F., Schekochihin, A. A., & Cowley, S. C. 2007, PhPl, 14, 100703
Madjarska, M. S., Huang, Z., Doyle, J. G., & Subramanian, S. 2012, A&A, 545, A67
Masuda, S., Kosugi, T., Hara, H., Tsuneta, S., & Ogawara, Y. 1994, Natur, 371, 495
Nagai, T., Shinohara, I., Fujimoto, M., et al. 2011, JGRA, 116, 4222
Ning, Z., Innes, D. E., & Solanki, S. K. 2004, A&A, 419, 1141
Nishizuka, N., Karlický, M., Janvier, M., & Bárta, M. 2015, ApJ, 799, 126
Peter, H., Tian, H., Curdt, W., et al. 2014, Sci, 346, C315
Petschek, H. E. 1964, in AAS-NASA Symp. on the Physics of Solar Flares, NASA-SP 50, ed. W. N. Hess (Washington DC: NASA), 425
Roussev, I., Doyle, J. G., Galsgaard, K., & Erdélyi, R. 2001, A&A, 380, 719
Savage, S. L., McKenzie, D. E., Reeves, K. K., Forbes, T. G., & Longcope, D. W. 2010, ApJ, 722, 329
Scherrer, P. H., Schou, J., Bush, R. I., et al. 2012, SoPh, 275, 207
Schmit, D. J., Innes, D., Ayres, T., et al. 2014, A&A, 569, L7
Sironi, L., & Spitkovsky, A. 2014, ApJL, 783, L21
Stone, J. M., Gardiner, T. A., Teuben, P., Hawley, J. F., & Simon, J. B. 2008, ApJS, 178, 137
Su, Y., Veronig, A. M., Holman, G. D., et al. 2013, NatPh, 9, 489
Uzdensky, D. A., Loureiro, N. F., & Schekochihin, A. A. 2010, PhRvL, 105, 235002
Winebarger, A. R., Emslie, A. G., Mariska, J. T., & Warren, H. P. 2002, ApJ, 565, 1298
Xiao, C. J., Wang, X. G., Pu, Z. Y., et al. 2006, NatPh, 2, 478